

# Excitonic Effects in Absorption Spectra of Carbon Dioxide Reduction Photocatalysts

Tathagata Biswas<sup>1</sup> and Arunima K. Singh<sup>1,\*</sup>

<sup>1</sup>Department of Physics, Arizona State University, Tempe, AZ, 85287

\*arunimasingh@asu.edu

## ABSTRACT

The formation and disassociation of excitons plays a crucial role in any photovoltaic or photocatalytic application. However, excitonic effects are seldom considered in materials discovery studies due to the monumental computational cost associated with the examination of these properties. Here, we study the excitonic properties of nearly 50 photocatalysts using state-of-the-art Bethe-Salpeter formalism. These  $\sim 50$  materials were recently recognized as promising photocatalysts for CO<sub>2</sub> reduction through a data-driven screening of 68,860 materials. Here, we propose three screening criteria based on the optical properties of these materials, taking excitonic effects into account, to further down select 6 materials. Remarkably we find a strong correlation between the exciton binding energies obtained from the Bethe-Salpeter formalism and those obtained from the computationally much less-expensive Wannier-Mott model for these chemically diverse  $\sim 50$  materials. This work presents a new paradigm towards the inclusion of excitonic effects in future materials discovery for solar-energy harvesting applications.

## Introduction

Excitons, which are quasiparticles, form when light is absorbed by semiconductors or insulators. They consist of a photoexcited electron and a hole bound by Coulomb interaction. In photocatalytic and photovoltaic processes these excitons must dissociate into free carriers and eventually reach the reacting species (in a photocatalytic process) or get converted into photocurrent (in a photovoltaic device) before any recombination processes can occur. Spontaneous generation of electron-hole (e-h) pairs from the dissociation of excitons is only possible when exciton binding energy (EBE) is lower than  $T\Delta S_{diss}$ , where  $T$  is the environmental temperature and  $\Delta S_{diss}$  is the entropy increase upon dissociation<sup>1</sup>. Once free e-h pairs are available, a low carrier recombination rate is desirable as it ensures most of these e-h pairs can be utilized in photocatalytic/photovoltaic applications. Both radiative, which are predominant in direct gap semiconductors, as well as non-radiative recombination processes have adverse effects on the quantum efficiency of a photocatalytic/photovoltaic device. However, with the help of innovative solutions such as use of multi-junction photocatalysts or solar cells<sup>2,3</sup> one can go beyond the limit set by radiative recombination processes. In the context of solar-cells, this limit is given by the Shockley–Queisser limit<sup>4</sup> and a lower limit is expected for photocatalysts<sup>5</sup>. Non-radiative recombinations that fall in the category of Shockley-Read-Hall<sup>6</sup> or trap-assisted recombinations can also be controlled by improving device quality and using defect-free semiconductors<sup>7</sup>. The other kind of non-radiative recombination, known as Auger recombination<sup>8,9</sup> is quite hard to eliminate<sup>10</sup>. High exciton binding energy is detrimental for a photovoltaic/photocatalytic device as it can facilitate these Auger recombination processes<sup>9,11</sup>. Therefore, it is important to consider excitonic effects while looking for promising photovoltaics and photocatalysts.

Excitonic effects have been seldom considered in material discovery studies conducted in the past for identifying promising photovoltaic or photocatalytic materials<sup>12–15</sup>. For instance, recently, Singh et. al.<sup>16</sup> performed the largest CO<sub>2</sub> photocathode search to date, where they shortlisted 52 materials starting from a list of 68,860 candidate materials. Their first-principles computation-based screening strategy was based on evaluating the thermodynamic stability, the electrochemical stability,<sup>17</sup> and the electronic structure compatibility with the CO<sub>2</sub> reduction reaction<sup>16</sup>. Their screening criteria were highly selective of robust photocatalysts when applied to the scores of known photocatalysts. However, despite its success, the screening did not incorporate any excitonic effects. In recent years, Bethe-Salpeter formalism (BSE) has gained remarkable success in probing excitonic effects in bulk<sup>18–20</sup> as well as 2-dimensional materials<sup>21–23</sup>, where these effects are more pronounced. The BSE formalism has a high computing resource requirement, both in terms of CPU time and memory. But, it has been found to have excellent agreement with experimental measurements across various materials classes.<sup>18–23</sup>

In this study, we design a materials screening strategy which is based on the optical properties and considers excitonic effects to identify the most efficient photocatalysts for CO<sub>2</sub> reduction among the 52 materials shortlisted by Singh et. al. We employ many-body perturbation theory within GW approximation together with<sup>24–26</sup> BSE to explore quasiparticle and optical properties. Our screening strategy involves three distinct properties —EBE of the materials, the capability to absorb incident

(visible or UV) radiation, and the degree of anisotropy in absorbing light of different polarizations. For each of these properties, we propose the limiting value for the criteria by looking at some of the well-known photocatalysts used for CO<sub>2</sub> reduction. Using these criteria we identify a shortlist of 6 suitable materials from Singh et al's study that display optical properties which are at par or better than known photocatalysts. This screening approach is broadly applicable to the discovery of materials for other solar-energy applications. The limiting value corresponding to each of the properties in such a screening strategy will, however, change based on the specific application.

As the BSE is computationally resource intensive and time-consuming, we also assess the prospect of using the computationally much less demanding Wannier-Mott model to compute the EBE of materials. We compare the EBE obtained from the BSE method and the Wannier-Mott model for 48 materials from Singh et al's study. These materials are chemically diverse—comprising of oxides, sulphides, tellurides, and arsenides. We find a strong correlation between the EBE obtained from the BSE and that obtained from the Wannier-Mott model. Thus, we surmise that the Wannier-Mott model can be used in place of the BSE method to estimate the EBE of materials in a computationally cheaper, hence potentially a high-throughput manner, to enable computational data-driven materials discovery for applications involving solar-absorption such as photovoltaics and photocatalysis.

## Results and Discussion

### GW-BSE vs HSE (Do we need GW-BSE?)

Singh et al.<sup>16</sup> had employed density-functional theory (DFT) with a hybrid exchange-correlation functional to compute the bandgaps and band edges of potential photocatalysts and identified materials that can utilize the visible-light spectrum which accounts for 44% of the solar radiation and simultaneously facilitate the reduction reaction of CO<sub>2</sub>. DFT which is designed to explore ground state properties suffers from bandgap underestimation problem as the bandgap is an excited state property of materials. Hybrid Functionals such as HSE and HSE06, overcome this issue by adding a fraction of Hartree-Fock exchange to the traditional exchange-correlation potential (LDA or GGA) and is quite successful in predicting correct bandgaps of a wide variety of materials. While hybrid functionals typically exhibit improved treatment of semiconductor bandgaps, they are heavily reliant on the fraction of the exact exchange included in the functional and are thus limited in their predictive capacity. This limitation is especially severe in the case of certain groups of materials where strong correlation effects are important, such as, transition metal oxides<sup>27</sup>.

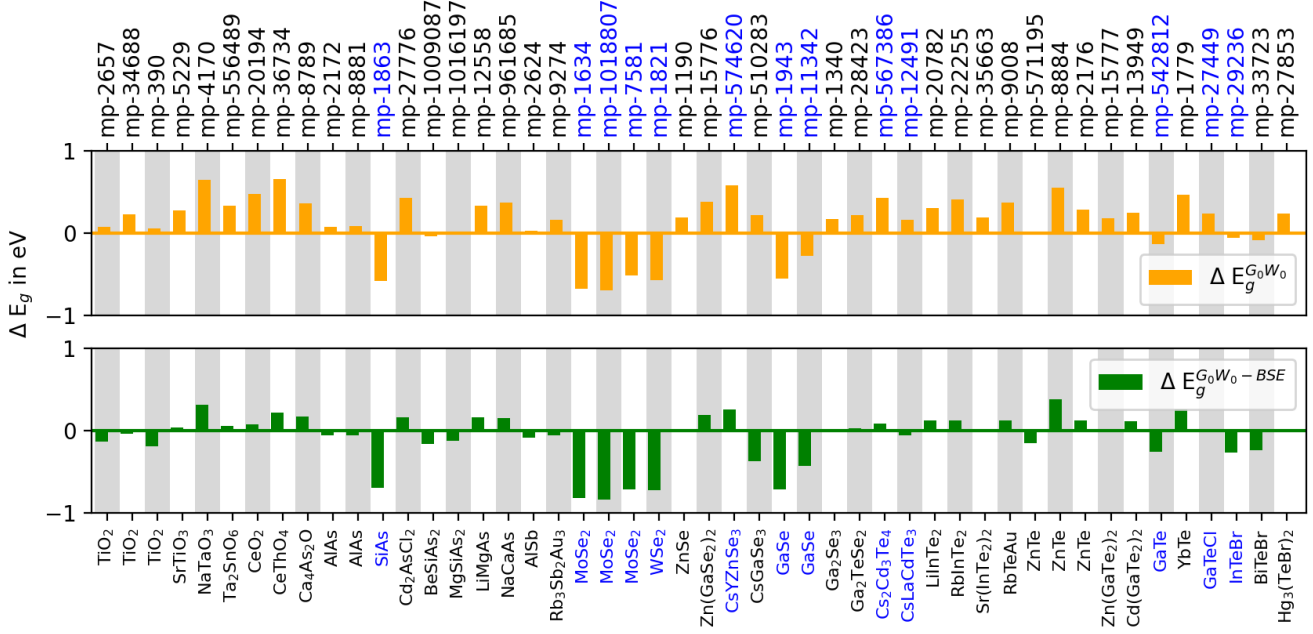
Many-body perturbation theory within GW approximation is often an order of magnitude more expensive than standard DFT with hybrid functionals but doesn't require any empirical parameters and is found to be remarkably successful in case of various materials classes. The GW formalism combined with BSE has been proven to be the state-of-the-art method to study the electronic structure and optical properties of a wide variety of semiconductor and insulator materials in recent years with an excellent predictive capacity.<sup>28–30</sup> Moreover, the GW-BSE computed absorption spectra have a very good agreement with experimentally measured spectra. Thus, we reevaluate the bandgaps of 48 photocatalysts from Singh et al's study using the GW method. We have restricted our study to the non-magnetic 48 of the 52 materials identified by Singh et al. We exclude the ZrVF<sub>6</sub> and the two phases of VOF as they have a magnetic ground state and the CdHgAsBr since it was found to be metallic according to our GW calculations.

Fig. 1 shows the difference between the HSE06 bandgaps,  $E_g^{\text{HSE}}$ , reported in Singh et al's work and the quasiparticle (QP) gaps obtained from  $G_0W_0$ ,  $E_g^{G_0W_0}$ , as well as the optical gaps obtained from  $G_0W_0$ -BSE,  $E_g^{G_0W_0\text{-BSE}}$  calculations. The difference between the quasiparticle gap of a material and its optical gap is precisely its EBE. One should note that,  $G_0W_0$  refers to non-self-consistent GW approximation. Here, the single-particle Green's function,  $G_0$ , and the screened Coulomb interaction,  $W_0$ , are calculated using Kohn-Sham eigenvalues and eigenfunctions<sup>31</sup>.

We have calculated a root mean square difference (RMSD), defined as  $\sqrt{\frac{1}{N}\sum_{i=1}^N(\Delta E_{g,i})^2}$ , for the gaps obtained from  $G_0W_0$  and  $G_0W_0$ -BSE with the HSE bandgap values for all the 48 materials. Where  $E_{g,i}$  is the bandgap of the  $i^{\text{th}}$  of the  $N=48$  materials considered in this study. Note that a positive  $\Delta E_{g,i}$  signifies underestimated HSE band gap. From Fig. 1 it is evident that except the layered materials, the HSE bandgap is almost always significantly underestimated compared to the QP gap obtained from  $G_0W_0$  calculations. We find an RMSD value of 0.16 eV for optical gaps and 0.31 eV for QP gaps for the non-layered materials considered in this study, which highlights the importance of studying photocatalytic materials with the GW-BSE methodology. In the case of layered materials, the difference between previously reported  $E_g^{\text{HSE}}$  and  $E_g^{G_0W_0\text{-BSE}}$  resulting from our calculation, has a different origin, which we will discuss in the following section.

### Layered materials and Van der Waals correction

We observe a large difference in the previously reported  $E_g^{\text{HSE}}$  values and our  $E_g^{G_0W_0}$  as well as  $E_g^{G_0W_0\text{-BSE}}$  values for the layered materials. This difference originates primarily from the change in the lattice parameters due to the Van der Waals



**Figure 1.** Differences between  $E_g^{\text{HSE}}$  and  $E_g^{G_0W_0}$  (orange) as well as  $E_g^{G_0W_0-BSE}$  (green). The Materials Project id's for each material noted on the bottom  $x$ -axis are listed on the top  $x$ -axis ticks. The layered materials have been labeled in blue.

mp-id	Formula	SG	$a^{\text{Theo}}$	$b^{\text{Theo}}$	$c^{\text{Theo}}$	$\alpha^{\text{Theo}}$	$\beta^{\text{Theo}}$	$\gamma^{\text{Theo}}$	$a^{\text{Expt}}$	$b^{\text{Expt}}$	$c^{\text{Expt}}$	$\alpha^{\text{Expt}}$	$\beta^{\text{Expt}}$	$\gamma^{\text{Expt}}$
mp-1863	SiAs	C2/m	16.15	3.72	9.64	90.00	105.76	90.00	15.98	3.67	9.53	90.00	106.00	90.00
mp-1943	GaSe	P6 <sub>3</sub> /mmc	3.80	3.80	15.73	90.00	90.00	120.00	3.75	3.75	15.99	90.00	90.00	120.00
mp-11342	GaSe	R3m	3.80	3.80	24.14	90.00	90.00	120.00	3.75	3.75	23.91	90.00	90.00	120.00
mp-542812	GaTe	C2/m	17.61	4.14	10.62	90.00	104.60	90.00	17.40	4.08	10.46	90.00	104.50	90.00
mp-1634	MoSe <sub>2</sub>	P6 <sub>3</sub> /mmc	3.33	3.33	13.17	90.00	90.00	120.00	3.29	3.29	12.93	90.00	90.00	120.00
mp-1018807	MoSe <sub>2</sub>	P6 <sub>3</sub> /mmc	3.32	3.32	13.06	90.00	90.00	120.00	3.28	3.28	12.92	90.00	90.00	120.00
mp-7581	MoSe <sub>2</sub>	R3m	3.33	3.33	19.78	90.00	90.00	120.00	3.29	3.29	19.39	90.00	90.00	120.00
mp-1821	WSe <sub>2</sub>	P6 <sub>3</sub> /mmc	3.31	3.31	13.04	90.00	90.00	120.00	3.28	3.28	12.96	90.00	90.00	120.00
mp-27449	GaTeCl	Pnmm	5.90	14.59	4.13	90.00	90.00	90.00	5.85	14.47	4.08	90.00	90.00	90.00
mp-29236	InTeBr	P2 <sub>1</sub> /c	7.46	7.70	8.32	90.00	115.45	90.00	7.35	7.58	8.34	90.00	117.61	90.00
mp-569454	CdHgAsBr	Pmma	5.17	8.93	9.80	90.00	90.00	90.00	4.70	8.79	9.78	90.00	90.00	90.00
mp-574620	CsYZnSe <sub>3</sub>	Cmcm	4.14	15.82	10.93	90.00	90.00	90.00	4.14	15.81	10.93	90.00	90.00	90.00
mp-567386	Cs <sub>2</sub> Cd <sub>3</sub> Te <sub>4</sub>	Ibam	6.74	13.16	15.56	90.00	90.00	90.00	6.67	13.01	15.39	90.00	90.00	90.00
mp-12491	CsLaCdTe <sub>3</sub>	Cmcm	4.66	17.32	12.17	90.00	90.00	105.60	4.64	16.70	12.17	90.00	90.00	90.00

**Table 1.** Comparison between the computed (Theo) and experimental (Expt) lattice constants ( $a$ ,  $b$ ,  $c$  in Å, and  $\alpha$ ,  $\beta$ ,  $\gamma$  in °), the Materials Project material ids (mp-id) and spacegroup (SG) of all the layered materials considered in this study. The experimental lattice constants are derived from the ICSD<sup>32</sup> as reported in the Materials Project database.

(vdW) corrections included in our work. Singh et. al. used the lattice parameters computed by the Materials Project for their computational screening of more than 68,000 potential candidates<sup>16</sup>. The Materials Project structural relaxation simulations do not account for any vdW corrections. For the layered materials, we have included van der Waals (vdW) corrections using the non-local van der Waals density functional (vdW-DF) proposed by Dion et al<sup>33</sup> with optimized exchange functionals (optB88)<sup>34</sup>.

In Table. 1 we compare the lattice parameters obtained by using vdW corrections for the structural optimization in case of the layered materials with the experimental lattice parameters and we find a very good agreement. The experimental lattice constants are obtained from the ICSD<sup>32</sup> lattice constants available through the Materials Project database. We also find that for these layered materials the Materials Project computed lattice parameters, and hence those used in Singh et al's work, are typically underestimated in the direction of the vdW bonding. This gives rise to larger  $E_g^{\text{HSE}}$  bandgaps in Singh et al's work and the significantly smaller  $E_g^{G_0W_0}$  and  $E_g^{G_0W_0-BSE}$  gaps in this work. A RMSD of 0.54 eV for optical gaps and 0.47 eV for QP gaps is observed for the layered materials considered in this study, underscoring the importance of vdW corrections. See

Supplementary Table S1 for the lattice parameters of all the 48 materials obtained from the vdW corrected functional.

In the case of the direct bandgap layered materials, GaSe and GaTe, the optical gap is found to be smaller than 1.7 eV, the lower end of the desirable 1.7 eV to 3.5 eV bandgap window of a visible-light photoabsorber.<sup>16</sup> For the dichalcogenides MoSe<sub>2</sub> (all three phases) and WSe<sub>2</sub> the direct absorption edge is just above 1.5 eV, however, at finite temperature the phonon assisted indirect absorption edge will be at an energy lower than 1.5 eV. These observations suggest that these materials may not be ideal for visible-light photocatalysis due to their low optical gap.

### **G<sub>0</sub>W<sub>0</sub> vs GW<sub>0</sub> (Which one is better?)**

We also computed the bandgaps using the partially self-consistent GW<sub>0</sub> and GW<sub>0</sub>-BSE calculations. In GW<sub>0</sub>, the eigenfunctions from ground-state calculations (i.e. DFT) are maintained, and G<sub>0</sub>W<sub>0</sub> calculations are performed to compute QP energies, which is then updated in the calculation of the Green's function, G<sup>26</sup>. These calculations show a significant increase in the QP gap for most of the oxides as well as several other materials such as CsYZnSe<sub>3</sub> and RbTeAu (see Supplementary Information Table S2). As a result, the RMSD value for the QP gap obtained from the GW<sub>0</sub> calculation shoots up to 0.8 eV. A relatively low RMSD value of 0.32 eV is obtained for the optical gap, as the EBE's are larger (~ 0.5 eV) for these materials.

Material	$E_g^{G_0W_0-BSE}$	$E_g^{GW_0-BSE}$	Experimental
TiO <sub>2</sub> (rutile)	3.07	3.91	3.03 <sup>35</sup>
TiO <sub>2</sub> (anatase)	3.31	4.19	3.42 <sup>36</sup>
SrTiO <sub>3</sub>	3.24	4.21	3.30 <sup>37</sup>
CeO <sub>2</sub>	3.68	6.04	3.78 <sup>38</sup>
MoSe <sub>2</sub>	1.08	1.14	1.09 <sup>39</sup>
WSe <sub>2</sub>	1.18	1.25	1.20 <sup>39</sup>
ZnSe	2.30	2.65	2.82 <sup>40</sup>
ZnTe	2.22	2.49	2.39 <sup>40</sup>
AlAs	2.04	2.26	2.15 <sup>41</sup>
AlSb	1.71	1.89	1.62 <sup>41</sup>

**Table 2.** Comparison between optical gaps obtained from G<sub>0</sub>W<sub>0</sub>-BSE,  $E_g^{G_0W_0-BSE}$ , GW<sub>0</sub>-BSE calculation,  $E_g^{GW_0-BSE}$ , and the experimental values previously reported in the literature. All values are in eV. The  $E_g^{G_0W_0-BSE}$  is in better agreement with the experimentally measured values in comparison to the  $E_g^{GW_0-BSE}$ .

Table 2 presents a comparison of the  $E_g^{G_0W_0-BSE}$  and  $E_g^{GW_0-BSE}$  with experimentally measured optical gaps. Experimental measurements of the optical gaps were available in the literature for 10 of the materials that we considered in this work – four oxides, three selenides, one arsenide, and an antimonide. The  $E_g^{G_0W_0-BSE}$  has a better agreement (RMSD=0.19 eV) with the experimentally obtained optical gaps than the  $E_g^{GW_0-BSE}$  (RMSD=0.86 eV). This might be due to the fact that the four oxides are wide bandgap materials and self-consistency tends to overestimate the bandgap in such materials<sup>42</sup>. The only materials for which the GW<sub>0</sub>-BSE provides better agreement with experiments is ZnSe and ZnTe. In case of MoSe<sub>2</sub> and WSe<sub>2</sub> self-consistency doesn't change the QP gap significantly and both G<sub>0</sub>W<sub>0</sub>-BSE and GW<sub>0</sub>-BSE provide excellent agreement with experiments. Therefore, in all the subsequent calculations reported in this study we have restricted ourselves with G<sub>0</sub>W<sub>0</sub> level of calculation to find the QP energies.

### **Design of the Screening Criteria**

We designed three screening criteria to identify the photocatalysts with the most suitable optical properties among the 48 materials considered in this study. Below we describe these criteria in detail.

#### **Criteria 1: Exciton Binding Energy**

As we have already discussed, high EBE is not desirable for photocatalytic or photovoltaic applications. Therefore, we consider materials that have an EBE of less than 200 meV as suitable candidates for photocatalysis. The motivation behind choosing 200 meV as the EBE criteria limit came from looking at the experimental EBE of materials that are currently accepted as a viable choice for photocatalytic applications, such as the anatase phase of TiO<sub>2</sub> (EBE=180 meV)<sup>43</sup> and MoS<sub>2</sub> (EBE=240 meV)<sup>44</sup>. We find that 26 of the 48 materials considered in this study have an EBE of less than 200 meV. We examine these materials in detail in the Outcome of Screening for Optical Properties section.

### Criteria 2: Average Integrated Absorption Coefficient

While it is necessary for a photoabsorber or photocatalytic material to have an optical gap in the visible light region to absorb a significant amount of sunlight, it is not a sufficient condition. It is also necessary that the material is able to absorb visible light of all possible polarizations. The amount of incident radiation of a certain frequency and polarization that will be absorbed by a material is determined by its absorption coefficient at that particular frequency and polarization axis.

Considering this, we propose to use an additional screening criteria to search for good photoabsorber/photocatalytic materials, one that is based on their integrated absorption coefficient,  $\alpha_{\text{int}}$ , for light polarization along the x ( $\parallel \hat{a}$ ), y ( $\parallel \hat{b}$ ) and z ( $\parallel \hat{c}$ ) crystal axes, namely  $\alpha_{\text{int}}^x$ ,  $\alpha_{\text{int}}^y$ , and  $\alpha_{\text{int}}^z$ .

$\alpha_{\text{int}}$  is computed by integrating the frequency dependent absorption coefficient ( $\alpha(\omega)$ ) in the 1.7-3.5 eV range<sup>16</sup> for a polarization of light along x ( $\parallel \hat{a}$ ), y ( $\parallel \hat{b}$ ) and z ( $\parallel \hat{c}$ ) axes. To compute  $\alpha(\omega)$  one needs both the real ( $\epsilon_1(\omega)$ ) and the imaginary ( $\epsilon_2(\omega)$ ) part of the dielectric function. In case of light polarization along x,

$$\alpha_{\text{int}}^x = \int_{\omega_{\text{min}}}^{\omega_{\text{max}}} \alpha^x(\omega) d\omega \quad \text{where} \quad \alpha^x(\omega) = \frac{2\pi |\sqrt{(\epsilon_1^x(\omega))^2 + (\epsilon_2^x(\omega))^2} - \epsilon_1^x(\omega)|}{\lambda} \quad (1)$$

where  $\omega$  and  $\lambda$  are the frequency and wavelength of incident radiation. Here, we obtain  $\epsilon_2(\omega)$  directly by solving BSE and use the Kramers–Kronig relation to calculate  $\epsilon_1(\omega)$ .

Through this integration of the  $\alpha(\omega)$  in the energy range of visible photons and averaging for different light polarization, one can eliminate all the materials that have excitons in the desired energy range but are optically inactive or ‘dark’. Optically ‘dark’ excitons exist as a solution to the BSE but have zero oscillator strength, hence, do not contribute to optical absorption.

To find a suitable cutoff value of  $\alpha_{\text{int}}^{\text{avg}}$  (defined as  $\frac{\alpha_{\text{int}}^x + \alpha_{\text{int}}^y + \alpha_{\text{int}}^z}{3}$ ) for identifying promising photocatalysts we again look at the most widely studied material for this application, the anatase phase of TiO<sub>2</sub>. However, the anatase TiO<sub>2</sub> is not used as a visible-light photocatalyst. The optimum performance for this material can only be achieved under exposure to UV radiation. Therefore, we have computed the  $\alpha_{\text{int}}^{\text{avg}}$  in the range of 3.5–4.2 eV for TiO<sub>2</sub> and used that as the cutoff. We find the value of  $\alpha_{\text{int}}^{\text{avg}}$  for TiO<sub>2</sub> is  $3.6 \times 10^4 \text{ cm}^{-1} \text{ eV}$ . This value is almost three times smaller than the  $\alpha_{\text{int}}^{\text{avg}}$  for silicon ( $10.5 \times 10^4 \text{ cm}^{-1} \text{ eV}$ ), the most widely used photoabsorber of this time. The  $\alpha_{\text{int}}^{\text{avg}}$  for silicon was computed using experimental data for  $\alpha(\omega)$ <sup>45</sup> in the visible range of 1.7–3.5 eV.

### Criteria 3: Anisotropy in Integrated Absorption Coefficient

Anisotropic absorption of light is undesirable as it would make certain surfaces of a poly-crystalline sample incapable of absorbing incident non-polarized solar radiation, and hence, reducing the efficiency of the solar-to-chemical energy conversion process. Thus, we consider an additional screening criteria,  $\alpha_{\text{int}}^{\text{aniso}}$ , that assess the anisotropy in the integrated absorption coefficients along x, y, and z polarization axis. Here,  $\alpha_{\text{int}}^{\text{aniso}} = \frac{\text{minimum}(\alpha_{\text{int}}^x, \alpha_{\text{int}}^y, \alpha_{\text{int}}^z)}{\text{maximum}(\alpha_{\text{int}}^x, \alpha_{\text{int}}^y, \alpha_{\text{int}}^z)}$ . By computing  $\alpha_{\text{int}}^{\text{aniso}}$  one can eliminate materials that absorb lights with preferential polarization. We chose an  $\alpha_{\text{int}}^{\text{aniso}}$  of  $> 0.8$  as the criteria of selection for this study.

In summary, the three criteria that we propose for screening photocatalysts with suitable optical properties are,

1. EBE  $< 200 \text{ meV}$
2.  $\alpha_{\text{int}}^{\text{avg}} > 3.6 \times 10^4 \text{ cm}^{-1} \text{ eV}$
3.  $\alpha_{\text{int}}^{\text{aniso}} > 0.8$

## Outcome of Screening for Optical Properties

### Exciton Binding Energy

In Fig. 2 we present the calculated optical gaps,  $E_g^{\text{G}_0\text{W}_0\text{-BSE}}$ , and the EBE of all the 48 materials. The bar heights denote the  $E_g^{\text{G}_0\text{W}_0\text{-BSE}}$  and their colors denote the exciton binding energy (EBE). Most of the oxides considered here have high EBE’s, making them unappealing for photovoltaic and photocatalytic applications. We, however, find 26 materials with very low EBE’s of  $< 200 \text{ meV}$ . The EBEs of all the 48 materials computed from both  $\text{G}_0\text{W}_0\text{-BSE}$  as well as  $\text{GW}_0\text{-BSE}$  are listed in the Supplementary Table S2.

With the exception of NaCaAs, all the materials considered in this study that have a  $\text{F}\bar{4}3\text{m}$  spacegroup (AlSb, AlAs, ZnTe, ZnSe, and LiMgAs) have EBE  $< 200 \text{ meV}$ . All of these materials have a Zinc-blend crystal structure except LiMgAs, which has an additional Mg atom at the center of the unit cell. AlAs and ZnTe with Wurtzite crystal structure (spacegroup  $\text{P6}_3\text{mc}$ ) also have quite low EBE’s, 145 meV and 169 meV respectively. Among the materials with low EBE ( $< 150 \text{ meV}$ ) we find two group-II–IV–V<sub>2</sub> ternary compounds with body centered tetragonal chalcopyrite structure (spacegroup  $\text{I}\bar{4}2\text{d}$ ) namely, MgSiAs<sub>2</sub> and BeSiAs<sub>2</sub>. These two materials are known to be promising materials for spintronics, electronic and

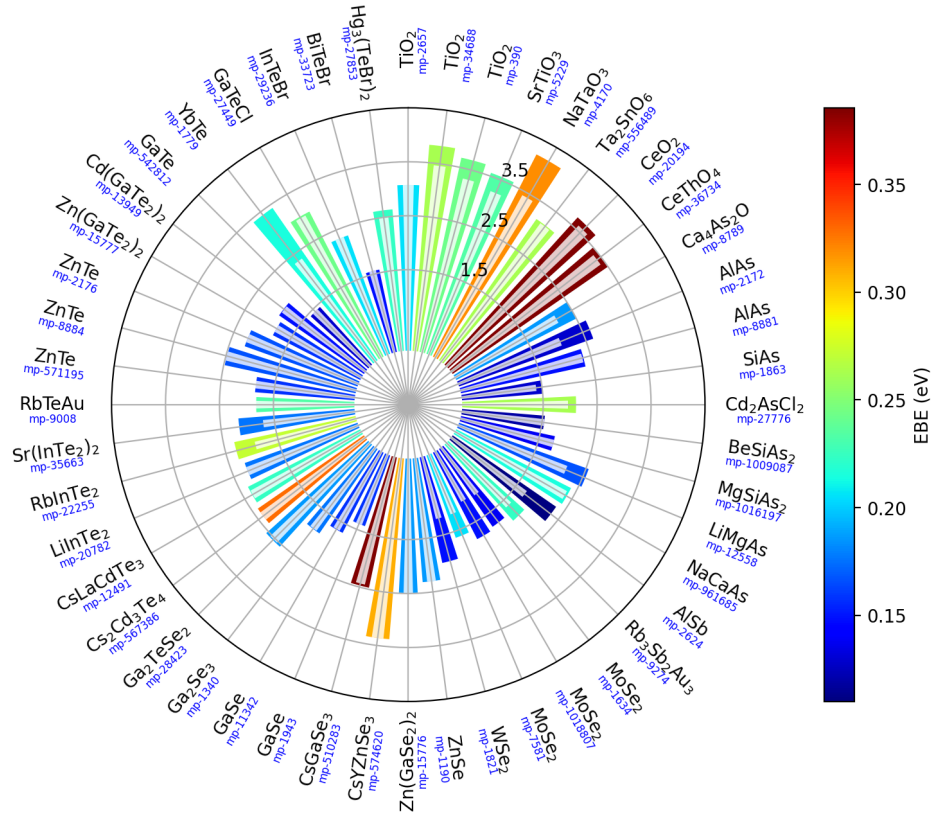


**Figure 2.** The bar heights denote the optical gap,  $E_g^{G_0W_0-BSE}$  in eV, and their colors denote the exciton binding energy (EBE) as obtained from  $G_0W_0$ -BSE calculations for the 48 materials. We find that 26 of the 48 materials have EBE less than 0.2 eV. The radial heights corresponding to 1.5 eV, 2.5 eV, and 3.5 eV optical gaps are labeled in the figure. The indirect absorption edges are shown as white bars for each material. For direct gap materials, they are equal to the optical gap.

optoelectronic applications such as infrared-nonlinear optical material, solar energy converters, infrared detectors, visible and invisible light-emitting diodes<sup>46,47</sup>.

A group of telluride materials ( $Zn(GaTe_2)_2$ ,  $Cd(GaTe_2)_2$ ,  $Sr(InTe_2)_2$ ), which are generally synthesized by preparing solid solutions of  $A_2Te_3$  ( $A = Ga, In$ ) with other  $A^{II}B^{IV}$  tellurides,<sup>48</sup> also exhibit low EBE's (140–180 meV). The layered chalcogenides (GaTe, GaSe, MoSe<sub>2</sub>, and WSe<sub>2</sub>) have EBE < 200 meV as well. Interestingly, the different phases of these chalcogenides do not have a significant effect on the EBE of these materials. Most of the layered dichalcogenides (MoSe<sub>2</sub>, WSe<sub>2</sub>) with hexagonal crystal unit cell (spacegroup  $P6_3/mmc$ ) have EBE in the range of (130–150 meV). MoSe<sub>2</sub> in a hypothetical phase with rhombohedral unit cell (spacegroup  $R3m$ ), that has a slightly larger EBE of 208 meV.

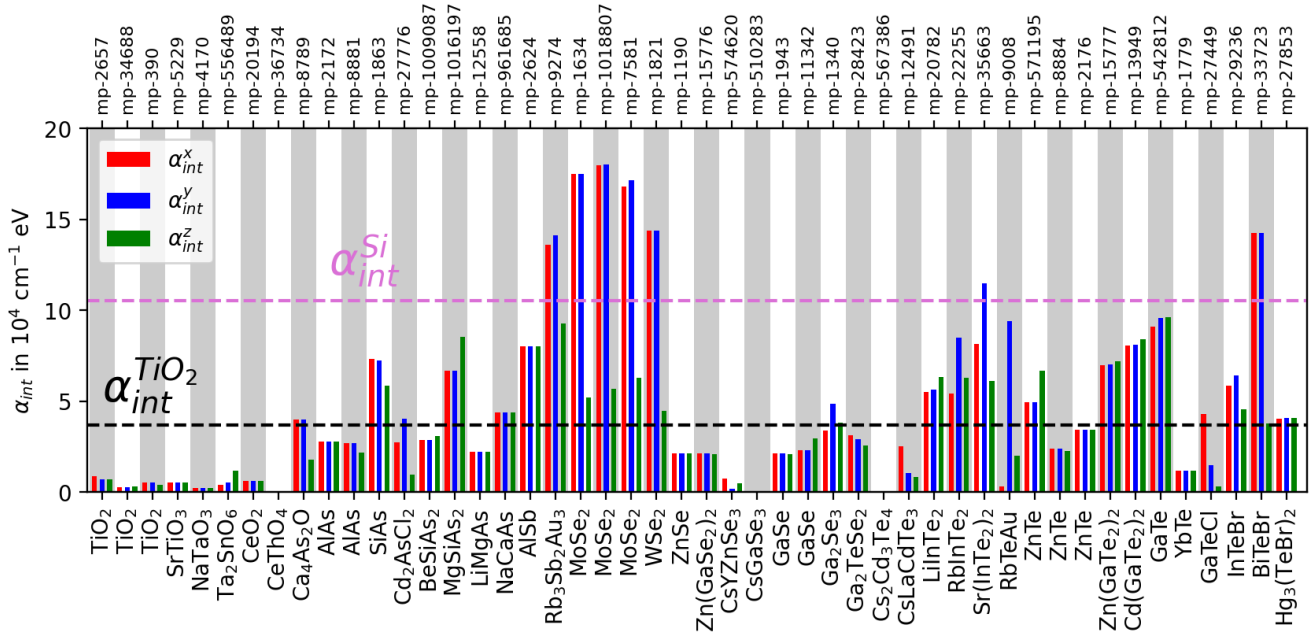
### Integrated Absorption Coefficient and Its Anisotropy

Fig. 3 shows the  $\alpha_{int}$  computed for the case of light polarization along  $x$  (red bars),  $y$  (blue bars), and  $z$  (green bars) axis for all 48 materials under consideration. We find that among materials with low EBE (< 200 meV) 14 materials that have a  $\alpha_{int}^{avg}$  values larger than the cutoff of  $3.6 \times 10^4 \text{ cm}^{-1} \text{ eV}$ .

In Fig. 4 we show the absorption spectra of four representative materials, BeSiAs<sub>2</sub> (mp-1009087), GaSe (mp-11342), BiTeBr (mp-33723) and AlSb (mp-2634). The excitation energies for each of these materials are shown as vertical lines in the yellow panels underneath their spectra.

Let us examine the case of BeSiAs<sub>2</sub>, Fig. 4a. For this material, we can see the lowest energy exciton is at 1.54 eV, its optical gap, and there are quite a few excitons in the 2-2.5 eV energy range. However, most of these excitons are 'dark', i.e. they do not yield an appreciable  $\alpha_{int}$ . Most of the 'bright' excitons for BeSiAs<sub>2</sub> lie above  $\sim 3$  eV and thus this material has a low  $\alpha_{int}$  value in the visible light region. Hence it does not meet the cutoff for criteria 2.

In the case of GaSe, which has a 1.67 eV optical gap, there are very few bright excitons below 2 eV and some bright



**Figure 3.** Integrated absorption coefficient ( $\alpha_{int}$ ) in case of light polarization along x (red bars), y (blue bars), and z (green bars) axis for all the materials under consideration. We have integrated the absorption coefficient over the 1.7-3.5 eV energy range to show the degree of anisotropy in absorption for the visible region of the solar spectrum. Horizontal dashed lines denote the  $\alpha_{int}$  values for silicon (magenta) and  $\text{TiO}_2$  (black).

excitons above 2.7 eV. The low number of excitons results in a poor  $\alpha_{int}$  value (Fig. 4b). Thus, this material also does not meet the criteria 2 cutoff.

Transition metal dichalcogenides  $\text{MoSe}_2$  and  $\text{WSe}_2$  and other layered material such as  $\text{BiTeBr}$  (Fig. 4c) absorb significantly poorly if the light polarization is along the z-axis ( $\sim 30\%$  compared to light polarization along x or y). This results in a low  $\alpha_{int}^{aniso}$  for many of the layered materials. For example,  $\text{GaTeCl}$  and  $\text{CsYZnSe}_3$  which are also layered materials show significantly lower absorption if the light polarization is along the axis with the vdW bonding. In the case of  $\text{GaTeCl}$  ( $\text{CsYZnSe}_3$ ) we see 66 (79) % and 92 (38) % decrease in total visible light absorption if the light polarization is along the y and z-axis respectively compared to if the polarization is along the x axis.  $\text{Ga}_2\text{Se}_3$ ,  $\text{RbInTe}_2$ ,  $\text{Sr}(\text{InTe}_2)_2$ ,  $\text{ZnTe}$ ,  $\text{Ta}_2\text{SnO}_6$  are some of the other materials which have a preference in absorbing visible lights of certain polarization than the others.

The absorption spectra of one of the gifted materials  $\text{AlSb}$  (mp-2634), which satisfies both the criteria 2 and 3 has been shown in Fig. 4d. It has an EBE of 110 meV,  $\alpha_{int}^{avg}$  of  $7 \times 10^4 \text{ cm}^{-1} \text{ eV}$ , and  $\alpha_{int}^{aniso}$  of 1.

The absorption spectra of all the 48 materials can be found in section VI of the Supplementary Information. Supplementary Table S4 lists the  $\alpha_{int}^{aniso}$ ,  $\alpha_{int}^{avg}$ ,  $\alpha_{int}^x$ ,  $\alpha_{int}^y$ , and  $\alpha_{int}^z$  in the visible-light (1.7–3.5 eV) range of all the 48 materials.

In Figure 5 we show a color-coded map to indicate which of the screening criteria are satisfied by the 48 materials. Materials that satisfy the EBE criteria are shaded in blue. Materials that satisfy both criteria 2 and 3 of meeting the cutoff of  $\alpha_{int}^{aniso}$  and  $\alpha_{int}^{aniso}$  in the visible light region (1.7–3.5 eV) are shaded in orange. Materials that satisfy criteria 2 and 3 in the UV region (3.5–4.2 eV) are shaded in green. In this color-coded map, we can see that only 6 materials meet the three criteria for visible light photocatalysis. These 6 materials are  $\text{AlSb}$ ,  $\text{SiAs}$ ,  $\text{GaTe}$ ,  $\text{Zn}(\text{GaTe}_2)_2$ ,  $\text{Cd}(\text{GaTe}_2)_2$ , and  $\text{LiInTe}_2$ . All of these materials have been previously synthesized.<sup>16</sup>  $\text{SiAs}$  and  $\text{GaTe}$  are layered materials. These layered materials can be extracted in two-dimensional forms, which are known to offer high specific surface area, tunability, and potential for heterostructuring.<sup>49–51</sup> In a recent computational study, Torrissi et al. have shown the two-dimensional  $\text{SiAs}$  is selective for CO production and has good absorption in the visible light region.<sup>49</sup> On the other hand, two-dimensional  $\text{GaTe}$  has been shown to exhibit a sharp decrease in photoluminescence during the transition from the many to few-layer limit.<sup>49</sup>

The materials that satisfy all the criteria in the UV region are markedly more, total 18. In Figure 5 these materials are shaded in blue and green colors. We observe that most of the oxides do not make the list but several arsenides, tellurides, and selenides emerge as suitable candidates. Supplementary Table S5 lists the  $\alpha_{int}^{aniso}$ ,  $\alpha_{int}^{avg}$ ,  $\alpha_{int}^x$ ,  $\alpha_{int}^y$ , and  $\alpha_{int}^z$  in the UV-light range (3.5–4.2 eV) of all the 48 materials.

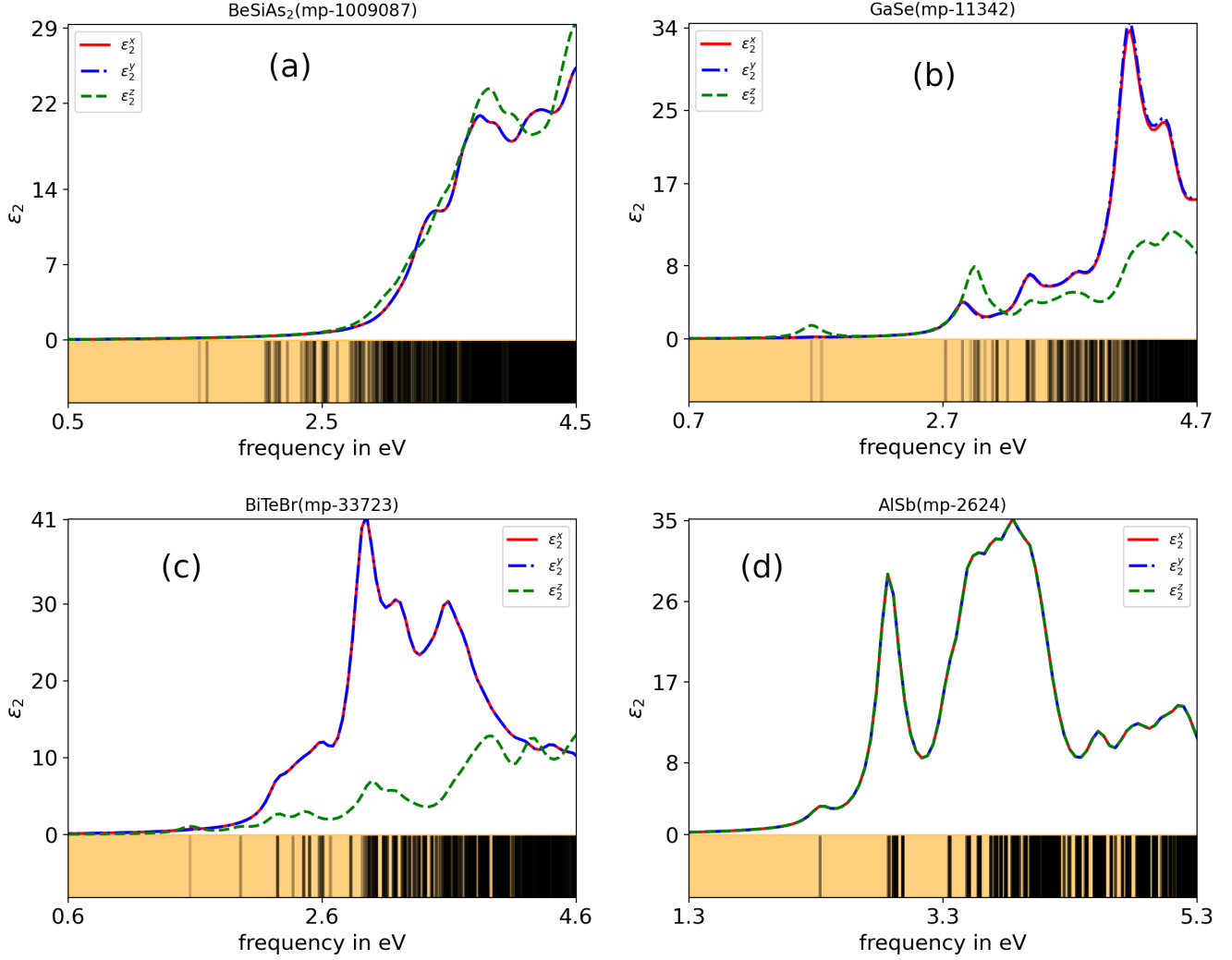


**Figure 4.** Imaginary part of the dielectric function for light polarization along  $x$  (red),  $y$  (blue) and  $z$  (green) axis obtained from  $G_0W_0$ -BSE calculation for (a)  $\text{BeSiAs}_2$  (mp-1009087), (b)  $\text{GaSe}$  (mp-11342), (c)  $\text{BiTeBr}$  (mp-33723), and (d)  $\text{AlSb}$  (mp-2624). The yellow panel on the bottom of each figure shows the excitation energies with vertical lines.

### Wannier-Mott Model vs BSE

In the case of most inorganic semiconductors, excitons can be approximated as an electron in the conduction band that is bound with a hole in the valence band through some form of screened Coulomb interaction and can be described using the Wannier-Mott (WM) model. This model uses effective mass approximation which describes electrons and holes as free particles having a parabolic dispersion and characterized by effective masses that depend on the crystal structure.

Within this approximation, the wave-function of relative electron-hole motion or exciton can be found from the Schrodinger equation very similar to the one describing the electron state in a hydrogen atom where we replace the electron mass,  $m_0$ , with reduced effective mass,  $\mu = \frac{m_e m_h}{m_e + m_h}$ , and replace the unscreened Coulomb interaction,  $\frac{e^2}{r}$ , between the electron-hole pair with the screened one,  $\frac{e^2}{\epsilon r}$ . Where  $m_e$  ( $m_h$ ) is the electron (hole) effective masses and  $\epsilon$  is the dielectric constant of the material. By solving the hydrogen atom like Schrodinger's equation we find the binding energy of the ground excited state ( $\text{EBE}_{\text{WM}}$ ),

$$\text{EBE}_{\text{WM}} = \frac{\mu e^4}{2\hbar^2 \epsilon^2} \quad (2)$$

Computationally it is much less expensive to obtain EBE using the WM model than solving the BSE. The input parameters in WM model are the dielectric constant and the effective masses, which can be obtained with reasonable accuracy using less



TiO <sub>2</sub> mp-2657	TiO <sub>2</sub> mp-34688	TiO <sub>2</sub> mp-390	SrTiO <sub>3</sub> mp-5229	NaTaO <sub>3</sub> mp-4170	Ta <sub>2</sub> SnO <sub>6</sub> mp-556489	CeO <sub>2</sub> mp-20194	CeThO <sub>4</sub> mp-36734
Ca <sub>4</sub> As <sub>2</sub> O mp-8789	AlAs mp-2172	AlAs mp-8881	SiAs mp-1863	Cd <sub>2</sub> AsCl <sub>2</sub> mp-27776	BeSiAs <sub>2</sub> mp-1009087	MgSiAs <sub>2</sub> mp-1016197	LiMgAs mp-12558
NaCaAs mp-961685	AlSb mp-2624	Rb <sub>3</sub> Sb <sub>2</sub> Au <sub>3</sub> mp-9274	MoSe <sub>2</sub> mp-1634	MoSe <sub>2</sub> mp-1018807	MoSe <sub>2</sub> mp-7581	WSe <sub>2</sub> mp-1821	ZnSe mp-1190
Zn(GaSe <sub>2</sub> ) <sub>2</sub> mp-15776	CsYZnSe <sub>3</sub> mp-574620	CsGaSe <sub>3</sub> mp-510283	GaSe mp-1943	GaSe mp-11342	Ga <sub>2</sub> Se <sub>3</sub> mp-1340	Ga <sub>2</sub> TeSe <sub>2</sub> mp-28423	Cs <sub>2</sub> Cd <sub>3</sub> Te <sub>4</sub> mp-567386
CsLaCdTe <sub>3</sub> mp-12491	LiInTe <sub>2</sub> mp-20782	RbInTe <sub>2</sub> mp-22255	Sr(InTe <sub>2</sub> ) <sub>2</sub> mp-35663	RbTeAu mp-9008	ZnTe mp-571195	ZnTe mp-8884	ZnTe mp-2176
Zn(GaTe <sub>2</sub> ) <sub>2</sub> mp-15777	Cd(GaTe <sub>2</sub> ) <sub>2</sub> mp-13949	GaTe mp-542812	YbTe mp-1779	GaTeCl mp-27449	InTeBr mp-29236	BiTeBr mp-33723	Hg <sub>3</sub> (TeBr) <sub>2</sub> mp-27853

**Figure 5.** The figure shows a color-coded map that indicates which of the screening criteria are satisfied by the 48 materials. The materials that satisfy the EBE criteria 1 are shaded in blue. The materials that satisfy both criteria 2 and 3 of meeting the cutoff of  $\alpha_{\text{avg}}^{\text{aniso}}$  and  $\alpha_{\text{int}}^{\text{aniso}}$  in the visible light region (1.7–3.5 eV) are shaded in orange. The materials that satisfy criteria 2 and 3 in the UV region (3.5–4.2 eV) are shaded in green.

the expensive DFT calculations<sup>52</sup>. Here, we test the applicability of WM model for the materials under consideration and the possibility of using WM instead of the expensive BSE calculations for future solar-materials discovery.

Note that the WM approximation is valid when the interaction potential is slowly varying over the dimension of a unit cell or in other words the dimension of the lowest energy exciton is much larger than the lattice dimension. In this case we get an EBE of the order of 0.2 eV. The EBE of the majority of the materials considered in this work is in the vicinity of 0.2 eV value, and the range of the EBE is 0.11–0.59 eV.

To find the degree of correlation between the EBE computed using BSE and WM model (EBE<sub>WM</sub>), we calculate the Pearson’s correlation coefficient (PCC) and the Spearman’s correlation coefficient (SCC)<sup>53</sup>. PCC indicates the strength of linear relationship between two variables whereas, SCC doesn’t assume any particular functional dependence to quantify the strength of the correlation. We find a PCC value of 0.77 and SCC value of 0.76 between the BSE EBE and the WM EBE, which suggests a strong correlation between the two. Therefore, it would be quite reasonable to use WM model for a computational data-driven discovery of materials that have low EBE instead of using the computationally much more expensive BSE calculations.

The high PCC value also suggests that we can scale the EBE obtained from WM model by a factor of 0.17 (see Supplementary Information Table S5) to get a reasonable prediction for the value obtained by solving the BSE. We find that such a scaling of the WM EBE to obtain the BSE EBE results in a mean squared error of 0.11 eV and root mean squared deviation of 0.12 eV, which is similar to the accuracy of standard GW-BSE calculation.

## Summary and Discussion

In summary, we have explored excitonic effects in the optical properties of 48 promising CO<sub>2</sub> reduction photocatalysts. We have designed a screening strategy considering the optical properties of materials that are crucial for such photocatalysts, i.e., the exciton binding energies, the capability to absorb visible light, and the degree of anisotropy in the absorption of light with different polarizations.

Using this screening strategy we have identified 6 materials that are suitable for visible light photocatalysis. Interestingly, to our knowledge, none of these materials have been extensively studied to be used as photocatalysts for CO<sub>2</sub> reduction. Three of these materials have been studied before using various theoretical and experimental methodology, i.e., SiAs<sup>54,55</sup>, AlSb<sup>56,57</sup>, and GaTe<sup>58</sup>. However, the other three materials LiInTe<sub>2</sub>, Zn(GaTe<sub>2</sub>)<sub>2</sub> and Cd(GaTe<sub>2</sub>)<sub>2</sub> have remained largely unexplored. It is noteworthy that all of these materials have been previously experimentally synthesized<sup>57,59–63</sup>. Our screening strategy also identifies 18 materials that are suitable for UV light photocatalysis.

Using the relatively large amount of the high-quality BSE EBE data generated in this work, we show that the Wannier-Mott model can be used for estimating excitonic binding energies in a computationally cheaper manner for large-scale computational material discovery of photoabsorber materials without the need of performing the extraordinarily expensive BSE calculations.

Overall, our work presents a new paradigm towards the inclusion of optical properties for data-driven discovery of materials

for solar energy conversion applications.

## Methods

All the first-principles calculations reported in this study were performed using Vienna Ab initio Simulation Package (VASP)<sup>31,64,65</sup>. The Kohn-Sham wavefunctions and eigenvalues were obtained using a plane wave basis with an energy cutoff of 520 eV. The exchange correlation functional was approximated using Generalized Gradient Approximation<sup>66</sup>. The Brillouin zone was sampled using a  $k$ -grid with 100 kpoints per  $\text{\AA}^{-3}$  of the reciprocal cell. The crystal structures were obtained by relaxing the atomic positions and the lattice parameters by a energy convergence cutoff of  $0.0005 \text{ eV} \times \text{number of atoms in the cell}$ , which has been found to produce well-converged structures in most instances<sup>67</sup>.

The macroscopic dielectric constants reported here were calculated using density functional perturbation theory following the formalism originally introduced by Baroni et. al.<sup>68</sup> and later implemented for projector-augmented wave methodology by Gajdoš et. al.<sup>52</sup>. The electron and hole effective masses were computed using parabolic line fitting at the direct band edges. We used the SUMO code<sup>69</sup> to perform the effective mass calculations.

The quasiparticle energies were obtained by using many body perturbations theory within both  $G_0W_0$  and  $GW_0$  approximation for the self-energy operator<sup>24,26,31</sup>. The basis set size for the response functions and  $W$  was chosen to include all plane waves up to an energy cutoff of 340 eV. The number of unoccupied bands included in the GW calculation was selected such that the QP gap is converged to within 0.1 eV. The excitonic effects were studied by solving Bethe-Salpeter equation within Tamm-Dancoff approximation<sup>65,70</sup>. We included all the occupied/unoccupied bands which were within 1.5 eV from band edges in the BSE calculation to ensure convergence of the absorption spectra. However, the convergence of the BSE absorption spectra with the number of  $k$ -points ( $N_k^{\text{BSE}}$ ) is often quite challenging and computationally expensive<sup>65</sup>. Nonetheless, in this study we selected the  $N_k^{\text{BSE}}$  such that the EBE converged to within 0.1 eV. See supplementary Table. S6 for a list of all the converged parameters for each of the 48 materials.

We have developed a Python code for performing automated first-principles calculations within GW-BSE framework and used it carry out all the calculations reported in this article. Our code is built upon open-source Python packages developed by the Materials Project, such as pymatgen<sup>71</sup>, fireWorks<sup>72</sup>, and atomate<sup>73</sup> to achieve complete automation of the entire multi-step GW-BSE computational framework that requires several convergence parameters. GW-BSE calculation is extremely sensitive to multiple interdependent convergence parameters such as number of bands ( $N_b$ ) included in the GW self energy calculation, number of  $k$ -points ( $N_k^{\text{BSE}}$ ) used to sample the Brillouin zone in the BSE calculation etc. Our workflow is capable of performing automated convergence test of all these parameters and using those values to carry out fully converged GW-BSE calculation. However, due to limitation of the computational resources available, we have restricted ourselves with converging  $N_b$  and  $N_k^{\text{BSE}}$ , two most sensitive parameters in the GW-BSE calculation. For several other convergence parameters such as, number of (imaginary) frequency grid points in GW calculation, energy cutoff for response function we have chosen a value large enough to produce quasiparticle energies within 0.1 eV. To reduce the computational cost associated with performing convergence tests we have judiciously used COHSEX and DFT level calculations which are significantly cheaper than full GW-BSE calculation. Details about these choices to perform efficient convergence calculations for GW-BSE calculations will be included in a forthcoming manuscript. In this workflow, we have also employed Wannier90<sup>71</sup>, a program for calculating maximally-localized Wannier functions to perform the interpolation required to obtain quasiparticle bandstructure.

## References

1. Giebink, N. C., Wiederrecht, G. P., Wasielewski, M. R. & Forrest, S. R. Thermodynamic efficiency limit of excitonic solar cells. *Phys. Rev. B* **83**, 195326 (2011).
2. Meng, A., Zhang, L., Cheng, B. & Yu, J. Tio<sub>2</sub>-mno x-pt hybrid multiheterojunction film photocatalyst with enhanced photocatalytic co<sub>2</sub>-reduction activity. *ACS applied materials & interfaces* **11**, 5581–5589 (2018).
3. Dimroth, F. & Kurtz, S. High-efficiency multijunction solar cells. *MRS bulletin* **32**, 230–235 (2007).
4. Shockley, W. & Queisser, H. J. Detailed balance limit of efficiency of p-n junction solar cells. *J. applied physics* **32**, 510–519 (1961).
5. Hashemi, S. M. H., Choi, J.-W. & Psaltis, D. Solar thermal harvesting for enhanced photocatalytic reactions. *Phys. Chem. Chem. Phys.* **16**, 5137–5141 (2014).
6. Shockley, W. & Read Jr, W. Statistics of the recombinations of holes and electrons. *Phys. review* **87**, 835 (1952).
7. Richter, A., Hermle, M. & Glunz, S. W. Reassessment of the limiting efficiency for crystalline silicon solar cells. *IEEE journal photovoltaics* **3**, 1184–1191 (2013).
8. Auger, P. Sur les rayons  $\beta$  secondaires produits dans un gaz par des rayons x. *CR Acad. Sci.(F)* **177**, 169 (1923).

9. Beattie, A. & Landsberg, P. Auger effect in semiconductors. *Proc. Royal Soc. London. Ser. A. Math. Phys. Sci.* **249**, 16–29 (1959).
10. Vossier, A., Hirsch, B. & Gordon, J. M. Is auger recombination the ultimate performance limiter in concentrator solar cells? *Appl. Phys. Lett.* **97**, 193509 (2010).
11. Yang, Y. *et al.* Comparison of recombination dynamics in  $\text{CH}_3\text{NH}_3\text{PbBr}_3$  and  $\text{CH}_3\text{NH}_3\text{PbI}_3$  perovskite films: influence of exciton binding energy. *The journal physical chemistry letters* **6**, 4688–4692 (2015).
12. Wang, H. *et al.* Insights into the excitonic processes in polymeric photocatalysts. *Chem. science* **8**, 4087–4092 (2017).
13. Guo, Z., Zhou, J., Zhu, L. & Sun, Z. Mxene: a promising photocatalyst for water splitting. *J. Mater. Chem. A* **4**, 11446–11452 (2016).
14. Shinde, A. *et al.* Discovery of manganese-based solar fuel photoanodes via integration of electronic structure calculations, pourbaix stability modeling, and high-throughput experiments. *ACS Energy Lett.* **2**, 2307–2312 (2017).
15. Yan, Q. *et al.* Solar fuels photoanode materials discovery by integrating high-throughput theory and experiment. *Proc. Natl. Acad. Sci.* **114**, 3040–3043 (2017).
16. Singh, A. K., Montoya, J. H., Gregoire, J. M. & Persson, K. A. Robust and synthesizable photocatalysts for  $\text{CO}_2$  reduction: a data-driven materials discovery. *Nat. communications* **10**, 1–9 (2019).
17. Singh, A. K. *et al.* Electrochemical stability of metastable materials. *Chem. Mater.* **29**, 10159–10167 (2017).
18. Umari, P., Mosconi, E. & De Angelis, F. Relativistic gw calculations on  $\text{CH}_3\text{NH}_3\text{PbI}_3$  and  $\text{CH}_3\text{NH}_3\text{SnI}_3$  perovskites for solar cell applications. *Sci. reports* **4**, 1–7 (2014).
19. Landmann, M., Rauls, E. & Schmidt, W. The electronic structure and optical response of rutile, anatase and brookite  $\text{TiO}_2$ . *J. physics: condensed matter* **24**, 195503 (2012).
20. Schmidt, F. *et al.* Quasiparticle and excitonic effects in the optical response of  $\text{KNO}_3$ . *Phys. Rev. Mater.* **3**, 054401 (2019).
21. Tran, V., Soklaski, R., Liang, Y. & Yang, L. Layer-controlled band gap and anisotropic excitons in few-layer black phosphorus. *Phys. Rev. B* **89**, 235319 (2014).
22. Ugeda, M. M. *et al.* Giant bandgap renormalization and excitonic effects in a monolayer transition metal dichalcogenide semiconductor. *Nat. materials* **13**, 1091–1095 (2014).
23. Qiu, D. Y., Felipe, H. & Louie, S. G. Optical spectrum of  $\text{MoS}_2$ : many-body effects and diversity of exciton states. *Phys. review letters* **111**, 216805 (2013).
24. Hedin, L. New method for calculating the one-particle green's function with application to the electron-gas problem. *Phys. Rev.* **139**, A796 (1965).
25. Hybertsen, M. S. & Louie, S. G. Electron correlation in semiconductors and insulators: Band gaps and quasiparticle energies. *Phys. Rev. B* **34**, 5390 (1986).
26. Shishkin, M. & Kresse, G. Self-consistent gw calculations for semiconductors and insulators. *Phys. Rev. B* **75**, 235102 (2007).
27. Viñes, F., Lamiel-García, O., Chul Ko, K., Yong Lee, J. & Illas, F. Systematic study of the effect of hse functional internal parameters on the electronic structure and band gap of a representative set of metal oxides. *J. computational chemistry* **38**, 781–789 (2017).
28. Onida, G., Reining, L. & Rubio, A. Electronic excitations: density-functional versus many-body green's-function approaches. *Rev. modern physics* **74**, 601 (2002).
29. Malone, B. D. & Cohen, M. L. Quasiparticle semiconductor band structures including spin-orbit interactions. *J. Physics: Condens. Matter* **25**, 105503 (2013).
30. Malashevich, A., Jain, M. & Louie, S. G. First-principles DFT + gw study of oxygen vacancies in rutile  $\text{TiO}_2$ . *Phys. Rev. B* **89**, 075205, DOI: [10.1103/PhysRevB.89.075205](https://doi.org/10.1103/PhysRevB.89.075205) (2014).
31. Shishkin, M. & Kresse, G. Implementation and performance of the frequency-dependent gw method within the paw framework. *Phys. Rev. B* **74**, 035101 (2006).
32. Belsky, A., Hellenbrandt, M., Karen, V. L. & Luksch, P. New developments in the inorganic crystal structure database (icsd): accessibility in support of materials research and design. *Acta Crystallogr. Sect. B: Struct. Sci.* **58**, 364–369 (2002).
33. Dion, M., Rydberg, H., Schröder, E., Langreth, D. C. & Lundqvist, B. I. Van der waals density functional for general geometries. *Phys. review letters* **92**, 246401 (2004).

34. Klimeš, J., Bowler, D. R. & Michaelides, A. Chemical accuracy for the van der waals density functional. *J. Physics: Condens. Matter* **22**, 022201 (2009).
35. Amtout, A. & Leonelli, R. Optical properties of rutile near its fundamental band gap. *Phys. Rev. B* **51**, 6842 (1995).
36. Tang, H., Levy, F., Berger, H. & Schmid, P. Urbach tail of anatase tio<sub>2</sub>. *Phys. Rev. B* **52**, 7771 (1995).
37. Tezuka, Y. *et al.* Photoemission and bremsstrahlung isochromat spectroscopy studies of tio<sub>2</sub> (rutile) and sr<sub>2</sub>tio<sub>3</sub>. *J. Phys. Soc. Jpn.* **63**, 347–357 (1994).
38. Griffiths, T. R., Davies, M. J. & Hubbard, H. V. S. A. Spectroscopic studies on single crystals having the fluorite lattice. part 1.—the fundamental absorption edge; urbach's rule and the debye temperature in ceo<sub>2</sub>. *J. Chem. Soc. Faraday Transactions 2: Mol. Chem. Phys.* **72**, 765–772 (1976).
39. Kam, K. & Parkinson, B. Detailed photocurrent spectroscopy of the semiconducting group vib transition metal dichalcogenides. *The J. Phys. Chem.* **86**, 463–467 (1982).
40. Pässler, R. *et al.* Temperature dependence of exciton peak energies in zns, znse, and znte epitaxial films. *J. applied physics* **86**, 4403–4411 (1999).
41. Madelung, O. *Semiconductors: data handbook* (Springer Science & Business Media, 2012).
42. van Schilfgaarde, M., Kotani, T. & Faleev, S. Quasiparticle self-consistent g w theory. *Phys. review letters* **96**, 226402 (2006).
43. Baldini, E. *et al.* Strongly bound excitons in anatase tio<sub>2</sub> single crystals and nanoparticles. *Nat. communications* **8**, 1–11 (2017).
44. Park, S. *et al.* Direct determination of monolayer mos<sub>2</sub> and wse<sub>2</sub> exciton binding energies on insulating and metallic substrates. *2D Mater.* **5**, 025003 (2018).
45. Green, M. A. & Keevers, M. J. Optical properties of intrinsic silicon at 300 k. *Prog. Photovoltaics: Res. Appl.* **3**, 189 – 192, DOI: [10.1002/pip.4670030303](https://doi.org/10.1002/pip.4670030303) (1995). <br />
46. Chiker, F., Kebbab, Z., Miloua, R. & Benramdane, N. Birefringence of optically uni-axial ternary semiconductors. *Solid state communications* **151**, 1568–1573 (2011).
47. Cheddadi, S. *et al.* First-principle calculations of structural, electronic, optical, elastic and thermal properties of MgXAs<sub>2</sub> (X = Si, Ge) compounds. *Pramana* **89**, 89 (2017).
48. Woolley, J. & Ray, B. Effects of solid solution of ga<sub>2</sub>te<sub>3</sub> with aii<sub>2</sub>vi tellurides. *J. Phys. Chem. Solids* **16**, 102–106 (1960).
49. Torrisi, S. B., Singh, A. K., Montoya, J. H., Biswas, T. & Persson, K. A. Two-dimensional forms of robust co<sub>2</sub> reduction photocatalysts. *npj 2D Mater. Appl.* **4**, 1–10 (2020).
50. Singh, A. K. & Hennig, R. G. Computational prediction of two-dimensional group-iv mono-chalcogenides. *Appl. Phys. Lett.* **105**, 042103 (2014).
51. Paul, J. *et al.* Computational methods for 2d materials: discovery, property characterization, and application design. *J. Physics: Condens. Matter* **29**, 473001 (2017).
52. Gajdoš, M., Hummer, K., Kresse, G., Furthmüller, J. & Bechstedt, F. Linear optical properties in the projector-augmented wave methodology. *Phys. Rev. B* **73**, 045112 (2006).
53. Weaver, K. F., Morales, V. C., Dunn, S. L., Godde, K. & Weaver, P. F. *An introduction to statistical analysis in research: with applications in the biological and life sciences* (John Wiley & Sons, 2017).
54. Wang, X. *et al.* A class of two-dimensional sias monolayers with novel electronic and optical properties from ab initio investigations. *The Eur. Phys. J. Plus* **134**, 287 (2019).
55. Kunioka, A., Ho, K. & Sakai, Y. Optical properties of sias single crystals. *J. Appl. Phys.* **44**, 1895–1896 (1973).
56. Wing, D. *et al.* Comparing time-dependent density functional theory with many-body perturbation theory for semi-conductors: Screened range-separated hybrids and the g w plus bethe-salpeter approach. *Phys. Rev. Mater.* **3**, 064603 (2019).
57. Blunt, R., Frederikse, H., Becker, J. & Hosler, W. Electrical and optical properties of intermetallic compounds. iii. aluminum antimonide. *Phys. Rev. (1,1893-132,1963/141,1966-188,1969)* **96**, 578–580 (1954).
58. Antonius, G., Qiu, D. Y. & Louie, S. G. Orbital symmetry and the optical response of single-layer mx monochalcogenides. *Nano letters* **18**, 1925–1929 (2018).

59. Wadsten, T. The crystal structure of si as. *Acta Chem. Scand.* (1-27,1973-42,1988) **19**, 1232–1238 (1965).
60. Julien Pouzol, M., Jaulmes, S., Guittard, M. & Alapini, F. Monotellurure de gallium, ga te. *Acta Crystallogr. B* (24,1968-38,1982) **35**, 2848–2851 (1979).
61. Kuehn, G., Schumann, B., Oppermann, D., Neumann, H. & Sobotta, H. Preparation, structure, and infrared lattice vibrations of li in te2. *Zeitschrift fuer Anorg. und Allgemeine Chemie (1950) (DE)* **531**, 61–66 (1985).
62. Errandonea, D. *et al.* X - ray diffraction study on pressure-induced phase transformations and the equation of state of zn ga2 te4. *J. Appl. Phys.* **114**, 233507–1–233507–7 (2013).
63. Neumann, H., Moise, E., Schwer, H. & Kramer, V. Infrared lattice vibrations of cd ga2 te4. *Cryst. Res. Technol.* **28**, 635–639 (1993).
64. Kresse, G. & Joubert, D. From ultrasoft pseudopotentials to the projector augmented-wave method. *Phys. review b* **59**, 1758 (1999).
65. Sander, T., Maggio, E. & Kresse, G. Beyond the tamm-dancoff approximation for extended systems using exact diagonalization. *Phys. Rev. B* **92**, 045209 (2015).
66. Perdew, J. P., Burke, K. & Ernzerhof, M. Generalized gradient approximation made simple. *Phys. review letters* **77**, 3865 (1996).
67. Jain, A. *et al.* A high-throughput infrastructure for density functional theory calculations. *Comput. Mater. Sci.* **50**, 2295–2310 (2011).
68. Baroni, S. & Resta, R. Ab initio calculation of the macroscopic dielectric constant in silicon. *Phys. Rev. B* **33**, 7017 (1986).
69. Ganose, A., Jackson, A. & Scanlon, D. sumo: Command-line tools for plotting and analysis of periodic\* ab initio\* calculations. *J. Open Source Softw.* **3**, 717 (2018).
70. Rohlfiing, M. & Louie, S. G. Electron-hole excitations and optical spectra from first principles. *Phys. Rev. B* **62**, 4927 (2000).
71. Mostofi, A. A. *et al.* wannier90: A tool for obtaining maximally-localised wannier functions. *Comput. physics communications* **178**, 685–699 (2008).
72. Jain, A. *et al.* Fireworks: A dynamic workflow system designed for high-throughput applications. *Concurr. Comput. Pract. Exp.* **27**, 5037–5059 (2015).
73. Mathew, K. *et al.* Atomate: A high-level interface to generate, execute, and analyze computational materials science workflows. *Comput. Mater. Sci.* **139**, 140–152 (2017).

## Data availability

All data supporting the findings of this work are available in the article and its Supplementary Information. Extra data and machine readable data are available upon reasonable request to the authors.

## Contributions

T.B performed the simulations and calculations. T.B. and A.K.S. analyzed the data and designed the research. Both the authors contributed to designing the research methods, interpreting the data, and writing the manuscript.

## Acknowledgements

This work was supported by the Arizona State University start-up funds and in part as part of ULTRA, an Energy Frontier Research Center funded by the U.S. Department of Energy (DOE), Office of Science, Basic Energy Sciences (BES), under Award # DE-SC0021230 (GW-BSE high-throughput simulations). In addition, Singh acknowledges support by the NSF DMR-grant NSF-DMR #1906030. The authors acknowledge the San Diego Supercomputer Center under the NSF-XSEDE Award No. DMR150006 and the Research Computing at Arizona State University for providing HPC resources. This research used resources of the National Energy Research Scientific Computing Center, a DOE Office of Science User Facility supported by the Office of Science of the U.S. Department of Energy under Contract No. DE-AC02-05CH11231.